Author/s:
Chen, D;Hudson, RJ;Tang, C;Sun, Q;Harmer, JR;Liu, M;Ghasemi, M;Wen, X;Liu, Z;Peng, W;Yan, X;Cowie, B;Gao, Y;Raston, CL;Du, A;Smith, TA;Li, Q

Title:
Colloidal Synthesis of Carbon Dot-ZnSe Nanoplatelet Van der Waals Heterostructures for Boosting Photocatalytic Generation of Methanol-Storable Hydrogen

Date:
2024

Citation:
Chen, D., Hudson, R. J., Tang, C., Sun, Q., Harmer, J. R., Liu, M., Ghasemi, M., Wen, X., Liu, Z., Peng, W., Yan, X., Cowie, B., Gao, Y., Raston, C. L., Du, A., Smith, T. A. & Li, Q. (2024). Colloidal Synthesis of Carbon Dot-ZnSe Nanoplatelet Van der Waals Heterostructures for Boosting Photocatalytic Generation of Methanol-Storable Hydrogen. Small, 20 (40), https://doi.org/10.1002/smll.202402613.

Persistent Link:
https://hdl.handle.net/11343/350212

RESEARCH ARTICLE

NANO · MICRO small
www.small-journal.com

Colloidal Synthesis of Carbon Dot-ZnSe Nanoplatelet Van der Waals Heterostructures for Boosting Photocatalytic Generation of Methanol-Storable Hydrogen

*Dechao Chen, Rohan J. Hudson, Cheng Tang, Qiang Sun, Jeffery R. Harmer, Miaomiao Liu, Mehri Ghasemi, Xiaomin Wen, Zixuan Liu, Wei Peng, Xuecheng Yan, Bruce Cowie, Yongsheng Gao, Colin L. Raston, Aijun Du, Trevor A. Smith, and Qin Li**

Methanol is not only a promising liquid hydrogen carrier but also an important feedstock chemical for chemical synthesis. Catalyst design is vital for enabling the reactions to occur under ambient conditions. This study reports a new class of van der Waals heterojunction photocatalyst, which is synthesized by hot-injection method, whereby carbon dots (CDs) are grown in situ on ZnSe nanoplatelets (NPLs), i.e., metal chalcogenide quantum wells. The resultant organic-inorganic hybrid nanoparticles, CD-NPLs, are able to perform methanol dehydrogenation through C–H splitting. The heterostructure has enabled light-induced charge transfer from the CDs into the NPLs occurring on a sub-nanosecond timescale, with charges remaining separated across the CD-NPLs heterostructure for longer than 500 ns. This resulted in significantly heightened H_2 production rate of 107 μmole·g^{-1}·h^{-1} and enhanced photocurrent density up to 34 μA cm^{-2} at 1 V bias potential. EPR and NMR analyses confirmed the occurrence of α-C–H splitting and C–C coupling. The novel CD-based organic-inorganic semiconductor heterojunction is poised to enable the discovery of a host of new nano-hybrid photocatalysts with full tunability in the band structure, charge transfer, and divergent surface chemistry for guiding photoredox pathways and accelerating reaction rates.

1. Introduction

The blueprint for the 'hydrogen economy' for reducing carbon emission requires efficient and cost-effective hydrogen storage and release but this remains technically and economically challenging.[1,2] Liquid organic hydrogen carriers (LOHCs) including ammonia, methanol, and various aromatic hydrocarbons offer viable solutions for H_2 storage and transport.[3,4] Among the various LOHC candidates, methanol, dubbed 'liquid sunshine', stands out as a cost-effective and high density energy carrier with low storage and transport costs for long-distance hydrogen transportation compared to liquid hydrogen and liquid methane.[5,6] The conventional methanol-based H_2 release process requires high temperature >200 °C, high pressure (20 – 50 bars) with the assistance of catalysts, and emits CO and CO_2 (CO_x). Room-temperature,

D. Chen, W. Peng, X. Yan, Q. Li
Queensland Micro- and Nanotechnology Centre
Griffith University
Nathan, QLD 4111, Australia
E-mail: Qin.li@griffith.edu.au

R. J. Hudson, T. A. Smith
ARC Centre of Excellence in Exciton Science & School of Chemistry
The University of Melbourne
Parkville, VIC 3010, Australia

C. Tang, Z. Liu, A. Du
School of Chemistry and Physics and Centre for Materials Science
Queensland University of Technology
Gardens Point Campus
Brisbane 4001, Australia

Q. Sun, J. R. Harmer
Australian Institute for Bioengineering and Nanotechnology
The University of Queensland
St Lucia, QLD 4072, Australia

M. Liu
Griffith Institute for Drug Discovery
Griffith University
Brisbane 4111, Australia

M. Ghasemi, X. Wen
School of Science
RMIT University
Melbourne, VIC 3000, Australia

B. Cowie
The Australian Synchrotron
Clayton, VIC 3168, Australia

The ORCID identification number(s) for the author(s) of this article can be found under https://doi.org/10.1002/smll.202402613

DOI: 10.1002/smll.202402613

photon-driven H_2 release from methanol has been demonstrated as a more controllable reaction without CO_x emission.[3] In methanol dehydrogenation, two reaction pathways are of high value, namely methanol to formaldehyde cyclable conversion[3,7] and methanol photo-reforming for simultaneous production of ethylene glycol and H_2.[8,9] The latter reaction requires activation of sp3 α-C–H in alcohol and C–C coupling, which is challenging since it is thermodynamically unfavorable, however, can be enabled by photocatalysis.[10,11] The ideal photocatalysts for achieving on-demand, efficient, light-controlled selective methanol dehydrogenation should exhibit high dispersity and photostability,[12,13] efficient photo-induced charge separation,[14] suitable surface polarity for preferential adsorption orientation, and adjustable redox potentials for selective methanol dehydrogenation pathways.[15,16]

Carbon dots (CDs) have received intense interest as a promising photocatalyst owing to their outstanding yet diverse optoelectronic properties, simple preparation methods, the applicability of circular chemistry, and boundless tunability through their physiochemical structural tweaking. CDs can be classified into a few subsets, namely carbon quantum dots (CQDs), amorphous CDs, graphene quantum dots (GQDs) and carbonized polymer dots.[17] The excited states of CQDs and GQDs, which involve sp^2 crystalline structures and show quantum effects, are most relevant to photocatalysis.[18,19] Elemental doping and the introduction of defects in CQDs have been demonstrated for band structure adjusting and charge carrier separation.[18,20] CQDs have also been physically mixed with other semiconductor materials for enhancing photocorrosion resistance[21] and tuning the electronic states[22]. Van der Waals (vdW) heterostructure usually refers to stackings of dissimilar 2D monolayers of semiconducting materials for tuning their electronic states and excitonic behaviour.[23] Though CQDs and GQDs are generally classified as 0D quantum materials, they can be viewed as pseudo 2D materials due to their distinctive planar structure. We hypothesize that incorporation of CQDs onto inorganic 2D quantum materials forming organic-inorganic vdW heterostructures will not only augment the tunability of the redox potential and enhance charge separation through charge transfer across interfaces, but also provide diverse surface chemistry for orientating the adsorbate molecules, hence providing means for driving different reaction pathways.

Colloidal heterostructures join two disparate nanomaterials intimately together using colloidal synthesis strategies, to tailor their properties for diverse functionalities and applications. Colloidal vdW heterostructure formation is expected to dramatically improve photocatalytic performance by modifying band structure, reducing recombination centres, increasing interfacial sites, and accelerating charge transfer.[24] The photocatalytic performance of quantum dot-based heterostructures is significantly dependent on the morphology of each component such as particle size and geometry, as well as the nature of the interface.[25–28] The nature of the interfacial contact between the two dissimilar nanomaterials is the key to tuning excitonic charge transport and catalytic activities.[27] However, growing nanoparticles on a heterointerface is challenging due to the competition of homogeneous nucleation in the solution phase, and lattice mismatch between two different materials. While significant progress has been made in the synthesis of metal-semiconductor hybrid nanosystems, that of CDs-semiconductor colloidal heterostructure is uncharted. Controlling the morphology and positional distribution of non-metal materials such as carbon on semiconductor nanoparticles is demanding due to the two disparate synthetic conditions and lattice mismatch of the two types of materials.[24,29] The high energy barrier of heterogeneous nucleation on the secondary component restricts the formation of carbon crystalline phases at the interface of the heterostructure. Thus far, CDs have not been able to form in situ vdW heterojunction photocatalysts with another semiconductor material, because of the wide dissimilarity between the organic and inorganic materials.

Herein, we report the colloidal synthesis of CD-ZnSe nanoplatelets (NPLs) heterostructures (CD-NPLs) via the hot-injection method. Highly crystalline CDs are in situ grown on the planar surfaces and the edges of ZnSe nanoplatelets (NPLs). By integrating optical characterizations and theoretical calculations, photoexcited electrons were found to flow from the CDs to NPLs, leaving holes on the CDs for activating α-C–H and C–C coupling, while transferring hot electrons onto the 2D nanoplatelets, which possess much higher interfacial surface area for H_2 reduction. The photoinduced charge separation in the CD-NPLs heterostructures occurs on a sub-nanosecond timescale, and these charges remain separated for hundreds of nanoseconds. The CD-NPLs heterostructures not only serve as an excellent photocatalyst for enabling CO_x-free methanol-based photocatalytic and photoelectrocatalytic (PEC) hydrogen generation, but also provide new catalyst designs for driving challenging reactions such as α-C–H activation and C–C coupling.

2. Results and Discussion

2.1. CD-NPLs Heterojunction Structure Design

We first constructed the CD-NPLs vdW heterostructure computational model with the density function theory corrected by DFT-D3 to describe the vdW interaction, **Figure 1a**.[10] The adsorption energy of the CDs is calculated to be -3.54 eV, indicating strong thermal stability ($>kT$). We present the density of states of the NPLs with CDs to illustrate the orbital hybridization in Figure 1b. Since the CDs are simulated by graphene fragments, the C p_x and p_y orbitals are coupled together to form intralayer π conjugation. Thus, the surface Zn p_{z2} orbital can directly hybridize with the C p_z orbital. The calculated vdW interactions between the CD and the surface Zn atoms are

Y. Gao
Institute for Integrated and Intelligent Systems
Griffith University
Nathan, QLD 4111, Australia
Y. Gao, Q. Li
School of Engineering and Built Environment
Griffith University
Nathan, QLD 4111, Australia
C. L. Raston
Flinders Institute for Nanoscale Science and Technology
College of Science and Engineering
Flinders University
Adelaide, SA 5001, Australia

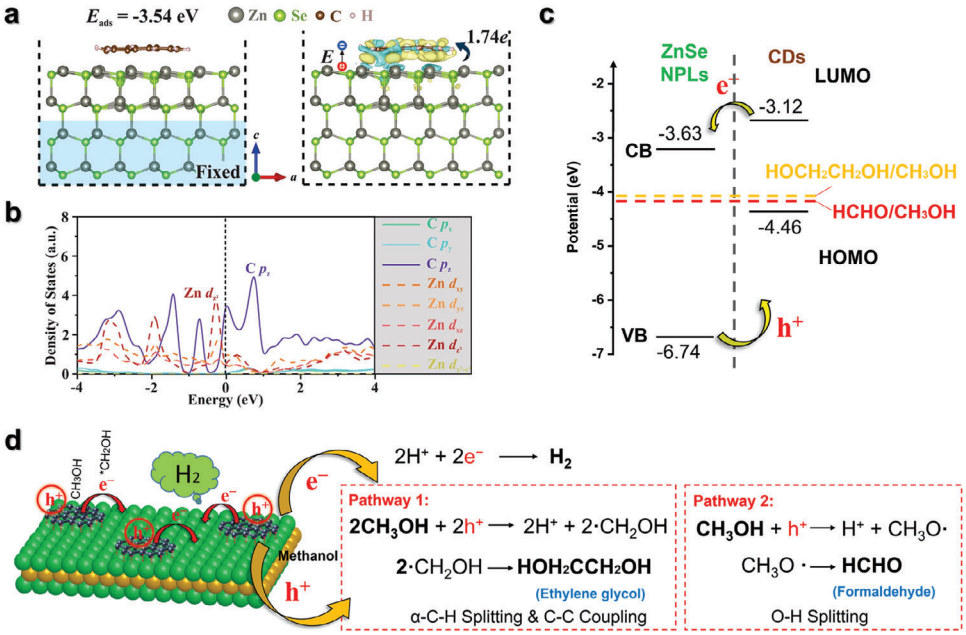

Figure 1. Design of colloidal CD-NPLs heterostructures. a) Optimized geometry of ZnSe (001) surface adsorbed with a carbon dot (grey, green, brown, and pink spheres representing Zn, Se, C and H atoms, respectively) along with charge density difference of carbon dots adsorbed on a ZnSe surface (yellow and cyan areas represent the electron accumulation and depletion, respectively). b) Orbital resolved density of states for carbon dots adsorbed ZnSe nano-plates. (calculated by the PBE functional). c) Band alignment of CD-NPLs heterostructures shows a Type-II heterojunction. d) The two possible pathways for methanol dehydrogenation and methanol molecule orientations on carbon dots and ZnSe NPL.

strong, resulting in an average interfacial distance of 2.28 Å. As shown in Figure 1b, the surface Zn d_{z2} orbitals and the p_z orbital of CDs are near the Fermi level overlap, which supports the significant interlayer charge redistribution. The calculated charge density difference, Figure 1a, indicates that the electrons are mainly accumulated around the CD and depleted from the Zn-termination. The inter-surface electron distribution leads to a built-in electric field pointing from the ZnSe substrate to the CD. The formation of this electric field will facilitate the transfer of excited electrons from the CDs to the ZnSe substrate. We then estimated electronic properties of the heterointerface with the electronic band structure calculated using the PBE0 method, showing a direct bandgap of 3.11 eV at the Γ point, Figure S1 (Supporting Information). The calculated band alignment shows that the conduction band (CB) of ZnSe is located between the highest occupied molecular orbital (HOMO) and the lowest unoccupied molecular orbital (LUMO) of the CDs, forming a type-II heterostructure, Figure 1c. The calculated HOMO energy level of the heterostructure is sufficient for oxidizing methanol. Such a band alignment is favorable for methanol dehydrogenation.

As indicated on Figure 1c, the methanol oxidation energies for the two reaction pathways, namely, 1.) methanol to formaldehyde: $CH_3OH \rightarrow H_2$ (g) + CH_2O; 2.) methanol to ethylene glycol and beyond: $CH_3OH \rightarrow HOCH_2CH_2OH + H_2$ (g), are not far apart. For reaction (2), the bottleneck is in the activation of inert sp3 α-C–H in alcohol and C–C bond formation. Therefore, reaction (1) is more prevailing. However, on the CDs-ZnSe NPLs heterostructure, the orientations of methanol molecules on the two disparate materials could be different as illustrated in Figure 1d; on CDs, the methanol molecules are more likely to attach with the CH_3 terminal, while on ZnSe NPLs, the methanol molecules are more likely to attach with the -OH terminal. This molecular orientation difference induced by catalyst surface polarity may play a role in guiding reaction pathways.

2.2. CD-NPLs Heterojunction Formation via the Hot-Injection Method

We employed the hot-injection method to in situ synthesize the CDs onto the ZnSe NPLs. Generally, the colloidal synthesis of citric acid-based carbon dots requires a higher temperature than the mild synthesis condition of ZnSe NPLs. However, it has been proven that the ZnSe NPLs will remain stable at 170 °C, but convert to nanorods at higher temperature, ~ 230 °C.[30,31] Hence, we chose the synthesis temperature of 170 °C for hot-injecting citric acid in oleyamine (OLA) stock solutions into ZnSe NPLs colloidal suspensions dispersed in OLA (procedures illustrated in Figure S2, Supporting Information). After quenching the reaction by adding methanol, the product solution was centrifuged at 5000 rpm (7 cm rotor radius; ~1,957 g). Since the CDs and the CD-NPLs heterostructure product have different solubilities in methanol, they spontaneously separate and the heterostructure product form a precipitate. Thus, centrifugation can effectively remove unattached CDs with the final product readily dispersed into organic solvents such as chloroform and methanol. The thermogravimetric analysis (TGA) determined the ratio of CDs/NPLs to be 0.156 (CDs = 12.5%, NPLs = 80%) in Figure S3 (Supporting Information). There are also about 7.5% (w/w) small molecules such as citric acid and OLA surface ligands attached on the surface of CD-NPLs.

The hot-injection method resulted in the carbonization of citric acid on the surface of ZnSe NPLs (**Figure** 2a; Figure

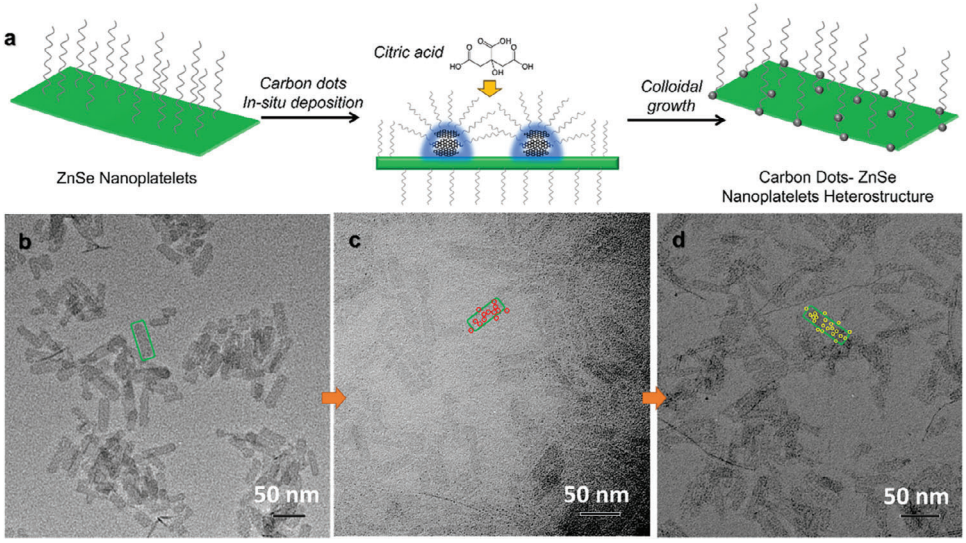

Figure 2. Synthesis of colloidal CD-NPLs heterostructures. a) Schematic of the in situ growth of CDs on the surface of ZnSe NPLs. The transmission electron microscopy (TEM) images of b) ZnSe NPLs, c) material extracted at 30 min after injection of citric acid, and d) the final CD-NPLs heterostructures 3 h after injection.

S2, Supporting Information). We used OLA as the solvent of choice since it can provide extraordinary spatial confinement for nanocarbon formation and introduce more bonding energy for CDs growth control, and, importantly, OLA is also compatible for the synthesis of ZnSe NPLs.[32,33] The average diameter of CDs on the NPLs surface is 3 nm (Figure 2b). The TEM images show that as-synthesized ZnSe NPLs have a uniform 2D layered structure. After 30 minutes of reaction, small clusters start to grow on the surface and after 3 hours they eventually grow over most of the polar surface of ZnSe NPLs (Figure 2c,d). Differing from the previous reports on the noble metal growth where particles can only grow on the edge of the nanoplatelets, the CDs appear to orient their sp^2 hybridized crystal plane favorably on the basal planes of the ZnSe NPLs which results in higher contact interface and increased loading ratio.[34–36]

2.3. Morphology of CDs-NPLs Heterostructure and Enhanced Crystallinity of CDs

In detail, the HAADF-STEM image shows a significant contrast between CDs and NPLs (**Figure** 3a,b). It clearly shows that the CDs have grown onto the surface of NPLs, and the CDs have an average diameter of 3.0 nm, Figure 3c. The NPLs are also confirmed to have an average length of 50 nm, a width of 16 nm and thickness of 1.39 nm (six atomic layers) (Figure 3a,d).[31] HRTEM establishes that the CDs are directly attached to the NPLs; there are no unattached CDs present (Figure 3d,e). The selected areas of f and in Figure 3e are enlarged, Figure 3f,h, showing the ZnSe NPLs with a single crystallinity of the (002) lattice plane.[31] The lattice plane spacings are measured to be 0.32 and 0.34 nm, which corresponds to the (002) and (100) planes of the ZnSe wurzite structure, respectively.[30,37] The thin edges of ZnSe NPLs are polarised, which is advantageous for the attachment of the CDs.[38] Figure 3h shows that the CDs, with a 0.26 nm lattice spacing corresponding to the (002) lattice plane of CDs, reside on both the lateral surface and edges of the NPLs with the boundary between the two materials clearly discernable in the HRTEM images. We note that the CDs have a more uniform size distribution compared to the CDs synthesized in ODE solvent.[32,33] The XRD, figure 3j, establishes that the crystallinity has been significantly increased compared to the CDs synthesized in ODE.[32] Interstingly, the CDs formed on the NPLs show a much more pronounced (002) plane peak attributed to carbon compared to the bare CDs. This suggests that the self-limitation and spatial confinement created by OLA reverse nanoemulsion can effectively provide localized, nanoscale, and sufficient temperature and pressure to graphitize citric acid as illustrated in Figure 2a, thereby increasing the crystallinity of the CDs.[33,39]

The choice of solvent is of critical importance in this in situ formation of CDs. Since the surfaces of ZnSe NPLs are stabilized by the potentially coordinating OLA ligands,[32] using OLA as the solvent for the heterostructure synthesis provides the surface ligand destabilization function for the CDs formation; this destabilization allows citric acid molecules to penetrate under the surface ligands, and to polymerize and dehydrate, in forming carbon nucleates and water molecules in localized high pressure regimes. OLA has been shown to provide extraordinary spatial confinement for nanocarbon formation due to its water tightness, with the amine terminal at the end of the alkane chain, and the bound water layer around the carbon nucleates, which results in directed growth of nanocarbon with a uniform size distribution, as illustrated in Figure 2a.[33] Moreover, from a thermodynamic point of view, such a heterostructure formation appears to follow the Volmer-Weber model, where the total Gibbs free surface energy is less than 0, i.e., $\Delta G_s < 0$, $\Delta G_s = \gamma_{1\_} \gamma_2 + \gamma_{1,2,}$ where γ_1 is the surface energy of the pre-existing material (ZnSe NPLs in OLA), γ_2 the surface energy of the growth

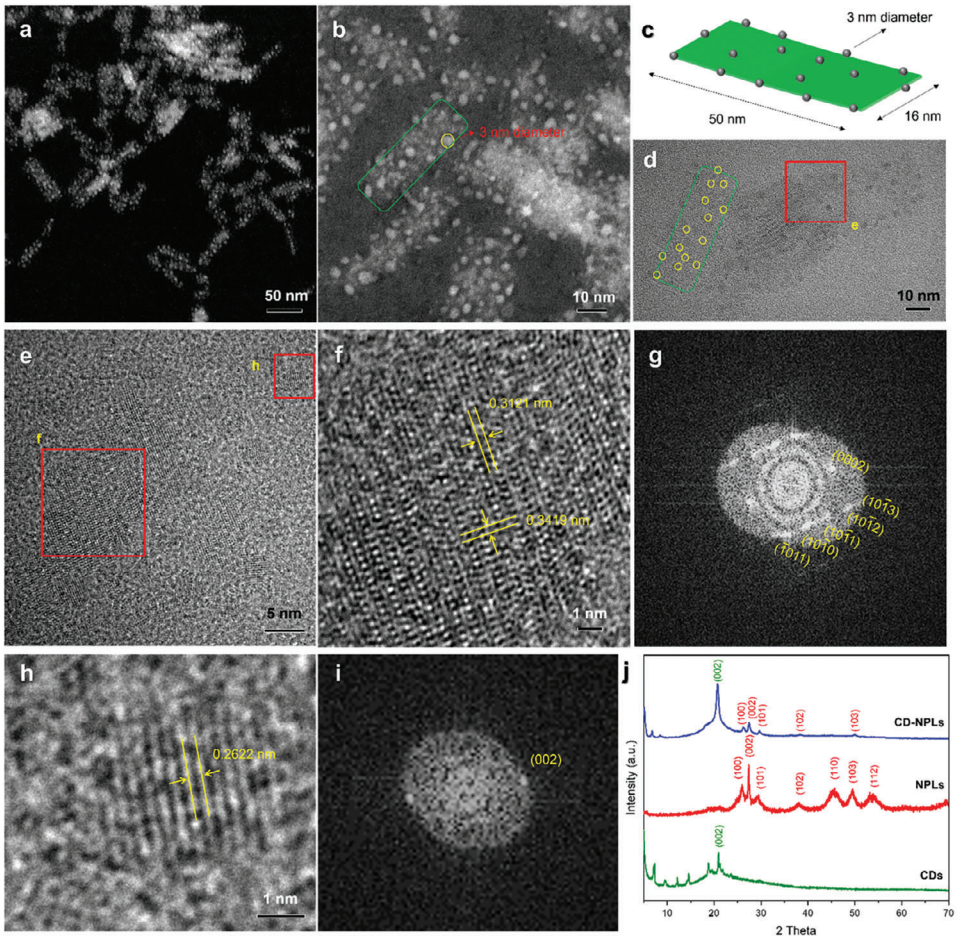

Figure 3. Structural characterization of CD-NPLs heterostructure. a,b) High-angle annular dark-field scanning TEM (HAADF-STEM) image of CD-NPLs heterostructure. c) Illustration of the size of CD-NPLs heterostructure. d,e) High-resolution transmission electron microscopy (HRTEM) images of CD-NPLs heterostructures. f,h) HRTEM images of the selected area in (e). g,i) Fast Fourier transform (FFT) patterns of the selected area in (e). j) X-ray diffraction (XRD) patterns of CDs, NPLs and CD-NPLs heterostructure.

material (CDs in OLA), and $\gamma_{1,2}$ the solid/solid interfacial energy.[40,41] This ligand-mediated nanocarbon formation on ZnSe NPLs provides a new pathway for organic-inorganic heterostructure material synthesis.

X-ray photoelectron spectroscopy (XPS) and near-edge X-ray absorption fine-structure spectroscopy (NEXAF) confirm the stability of the CDs, Figure S4 (Supporting Information). The XPS shows no shift on the Zn between NPLs and CD-NPLs, Figure S4a (Supporting Information). The XPS C spectra of CDs and CD-NPLs show a consistent ratio on the C–C/C=C, C-O and C=O bonding (Figure S4b, Supporting Information). The NEXAF spectra in the C K-edge reveal the dipole transitions from C 1s core states to 2p-derived electronic states of CDs. Figure S4c (Supporting Information) exhibits sharp feature peaks at 285, 288 and 291 eV, which are attributed to the C 1s transitions of π^* C=C, π^* C=O and σ^* C–C states, respectively.[42] Overall, the evidence confirms that the CDs are stably adhered on the ZnSe NPLs without chemical bonding in between, forming a stable colloidal 0D-2D vdW heterostructure.

2.4. Photoinduced Charge Separation in the CD-NPLs Heterostructure

Steady-state absorption and photoluminescence (PL) spectra of CDs, NPLs and CD-NPLs are shown in **Figure** 4a. The neat NPLs exhibit two sharp absorption peaks at 325 and 343 nm, with emission onset around 400 nm. The neat CDs show similar absorption features, with broader absorption bands at 365 and 380 nm, and an absorption tail that extends out to 450 nm. Rather than a direct linear addition of these two spectra, the absorption of the CD-NPLs composites shows a broadening and redshift in the main NPLs absorption bands, suggesting that the formed CDs influence the electronic structure of the NPLs. A raised baseline throughout the visible region is also evident for the NPLs and CD-NPLs, consistent with significant Rayleigh scattering of light from these particles. The PL spectrum of CD-NPLs also shows intimate interactions between the CDs and ZnSe NPLs. As depicted in Figure 4b, there is nearly no PL peak observed for the neat NPLs throughout the visible region,[43,44] whilst the bare CDs show a strong emission band centered at

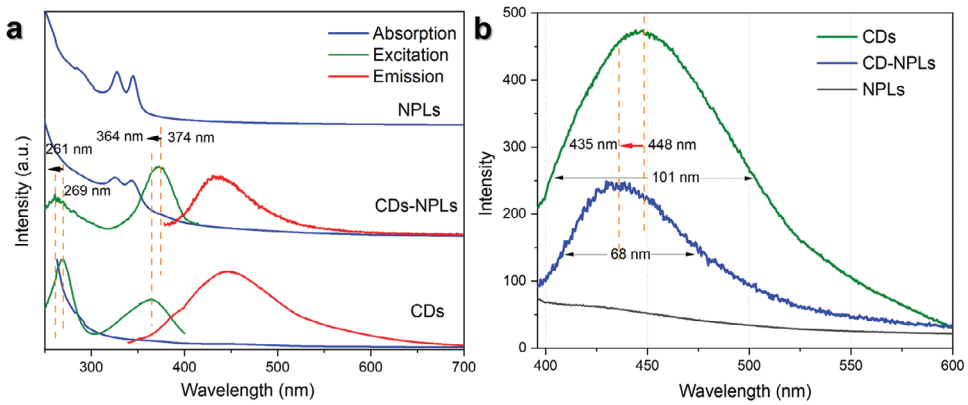

Figure 4. Optical properties of colloidal CD-NPLs heterostructures. a) Normalized absorption, PL and PL excitation (PLE) spectra of CDs, NPLs and CD-NPLs. b) PL spectra of CDs, NPLs and CD-NPLs of the same concentration excited at 400 nm.

448 nm. Distinctively, the PL spectrum of CD-NPLs not only shows a narrower full-width at half-maximum (FWHM) reduced from 101 to 68 nm and almost halved intensity compared with that of bare CDs, but also a 13 nm blue shift in its emission peak. The two emission centres at 261 and 364 nm in bare CDs, have also been reduced to a singular peak at 374 nm in CD-NPLs (PLE in Figure 4a). The diminishing of the 269 nm peak suggests that the higher energy transition of the CDs has become prohibited by the attachment of the NPLs. The quantum yield of CD-NPLs was determined as 11%, significantly reduced from that of the bare CDs, 57%. The modifications in the optical properties of CD-NPLs indicate that the colloidal CD-NPLs exhibit vdW heterostructure features, where the close proximity between the CDs and ZnSe NPLs has resulted in electronic interactions between these components, and electron transfer may therefore be possible between them,[45] as the computational model predicted.

To test for possible charge transfer between CDs and NPLs, time-resolved PL of the CDs and CD-NPLs was collected using time-correlated single photon counting (TCSPC), upon 400 nm excitation, where the NPLs absorption is effectively negligible and the recorded PL features can be solely attributed to CDs emission. The PL decays faster in the CD-NPLs than in the bare CDs (Figure S5, Supporting Information), which suggests that the excited state of the CDs is quenched by some non-radiative relaxation process induced by the NPLs, indicating charge transfer between the CDs and the NPLs. While the CDs emission decay can be well fitted by a biexponential decay function, a triexponential model is necessary to adequately fit the PL dynamics from the CD-NPLs (best-fit parameters for these emission decays are shown in Table S1, Supporting Information). The additional fast decay component in the CD-NPLs dynamics ($\tau_3 \approx 0.48$ ns) indicates that this non-radiative depopulation of the CDs emissive excited state occurs on a sub-nanosecond timescale.

2.5. Excited-State Behavior of Colloidal CD-NPL Heterostructures

Transient absorption (TA) spectroscopy was used to characterize charge dynamics of these materials on the femtosecond-nanosecond timescale. The TA spectra of neat CDs in chloroform (chloroform was used due to better dispersity), **Figure** 5a, show two spectral features immediately after excitation (<1 ps delay): the edge of a stimulated emission (SE) band at 480–500 nm and a broad excited-state absorption (ESA) signal centered around 650 nm. This ESA band decays on a sub-picosecond timescale, with a new ESA feature at 500 nm growing concurrently. After a rapid initial interconversion, this process continues more slowly on a timescale of tens of picoseconds, with an isosbestic point observed between these two ESA features at 525 nm over this timescale (Figure S6a, Supporting Information). The 500-nm ESA then decays on a nanosecond timescale, with concomitant broadening of the 550–600 nm ESA band. Finally, all remaining signals decay over several nanoseconds, agreeing with the emission kinetics of these CDs observed using TCSPC. Single-wavelength kinetic traces of the two ESA bands (Figure 5c,d) indicate time regimes on the order of 0.5 ps, 10 ps, 500 ps and 4 ns upon excitation. Drawing upon previous studies of comparable CD systems, we assign these timescales (in order of increasing timescale) as corresponding to: optical phonon scattering, acoustic phonon scattering, non-radiative carrier recombination and radiative carrier recombination.[46]

Photoexcitation of the CD-NPL composite at 400 nm excites only the CDs component of this material; neat NPLs show no significant absorption at this wavelength, and 400-nm excitation of neat NPLs results in negligible TA signal. TA spectra of CD-NPLs upon 400-nm excitation (Figure 5b) are initially similar to those of the neat CDs, showing the broad ESA at 650 nm and the SE edge at <500 nm before a sub-picosecond interconversion into the ESA at 500 nm. However, beyond 50 ps delay time the TA dynamics of the composite material diverge significantly from those of the bare CDs, with both ESA bands in the CD-NPLs sample decaying over hundreds of picoseconds. This timescale is consistent with the additional decay component fit to the PL decay in this system, and so again suggests that the presence of NPLs introduces an additional exciton quenching pathway on a timescale of approximately 500 ps. In addition, the TA spectra of CD-NPLs do not decay to the baseline, but are replaced by a broad, long-lived negative signal which extends across the visible region and persists for all remaining delay times accessible in this experiment (Figure 5b, 500–5000 ps). Negative TA signals correspond

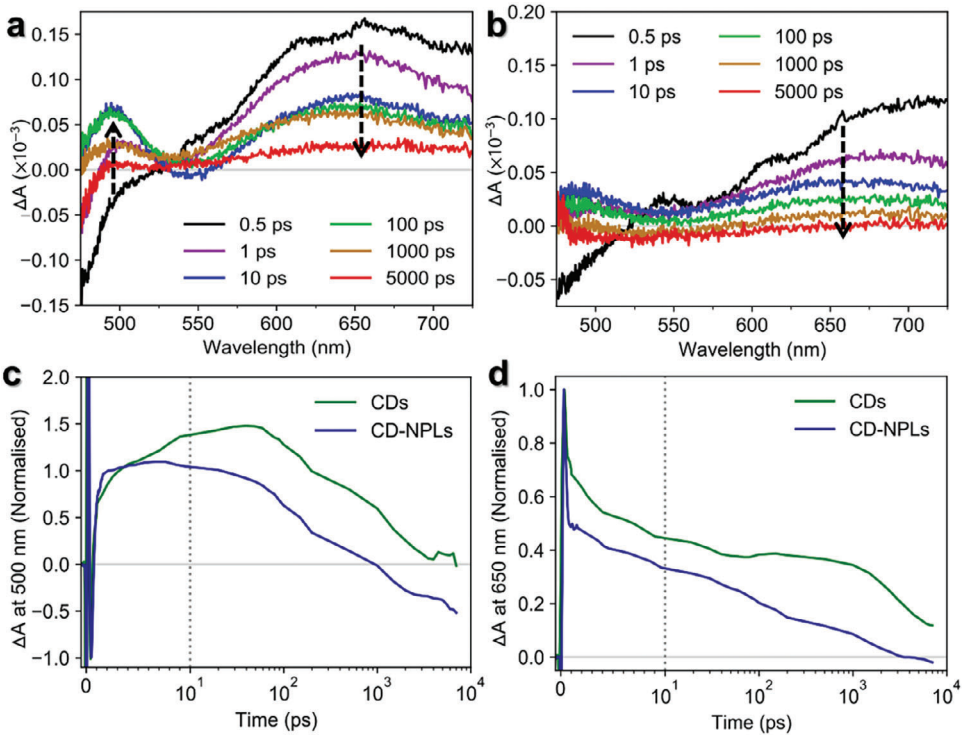

Figure 5. Transient absorption (TA) of colloidal CD-NPLs heterostructures. TA spectra of a) CDs at different delay times after excitation at 400 nm, b) CD-NPLs at different delay times after excitation at 400 nm. Normalized single-wavelength kinetic traces at c) 500 nm and d) 650 nm for CDs and CD-NPLs in chloroform upon 400 nm excitation.

to either SE or ground-state bleaching (GSB), but the lack of any CD-NPLs steady-state absorption features in this spectral region excludes the possibility of this signal arising from GSB. Therefore, this negative-going signal must arise from some form SE. Upon comparison to the steady-state PL features of these samples, this SE signal closely resembles the weak, broad emission of the neat NPLs (Figure 4a). Further TA experiments confirm this, with the excitation of neat NPLs at 350 nm yielding a similar long-lived SE band in the visible region (Figure S7, Supporting Information).

As mentioned above, NPL absorption at 400 nm is effectively negligible and neat NPLs exhibit no resolvable TA signal upon excitation at this wavelength. The emergence of a NPLs SE band upon excitation of CD-NPLs at 400 nm is therefore suggestive of charge transfer from the CDs into the NPLs, followed by trapping and radiative recombination at NPL trap or defect sites. This is supported by the sub-nanosecond PL quenching and decay of CD ESA features in the CD-NPL TA spectra (Figure 5c,d), indicating that deposition of CDs onto NPLs results in a rapid depopulation of the CD excited state through charge transfer into the NPL conduction band. These separated charges then persist for at least several hundred nanoseconds (Figures S8–S11, Supporting Information). Such a long charge carrier separation time fits with the characteristics of vdW excitonic materials.[23] This kind of rapid charge separation across the CD-NPLs heterostructure followed by long-lived charges are favorable for driving photocatalytic reactions under UV irradiation.[24]

2.6. Photo-Driven H_2 Generation from Methanol

Two modes of light-triggered hydrogen release from methanol at room temperature and one atmosphere are demonstrated herein, namely photoelectrocatalytic- and photocatalytic-dehydrogenation. The PEC response was tested at open circuit potential (OCP) and different bias potentials (0.1 and 1 V) under chopped illumination at 1.0 V against Ag/AgCl electrode in 0.1 M KOH methanol solution, **Figure** 6a. The CD-NPLs photoelectrode generated a 0.8 μA cm^{-2} at OCP, 5 μA cm^{-2} at 0.1 V and 34 μA cm^{-2} at 1 V, while the photoanodes made with CDs and NPLs on their own produced no photocurrent. The significant improvement of photocurrent density in the CD-NPLs suggests efficient electron-hole separation and enhanced interfacial redox reactions.

The photocatalytic H_2 generation performance was tested by comparison of CDs, NPLs and CD-NPLs in a dispersion under xenon light irradiation. CD-NPLs show the highest H_2 production efficiency of 107 μmole·g^{-1}·h^{-1}, 4 times higher than the yield compared to that enabled by the bare CDs (Figure 6b). This is likely due to the significantly improved charge separation, as demonstrated by the TA results. Similarly, NPLs exhibited less promotion on the H_2 generation compared to CDs. Interestingly, a mixture of CDs and NPLs shows even lower efficiency compared with each component on their own, which is likely due to reduced light irradiation on the photocatalytically active population, Figure 6c. The photocatalyst is only sensitive to the UV range of 250–400 nm with an Apparent Quantum

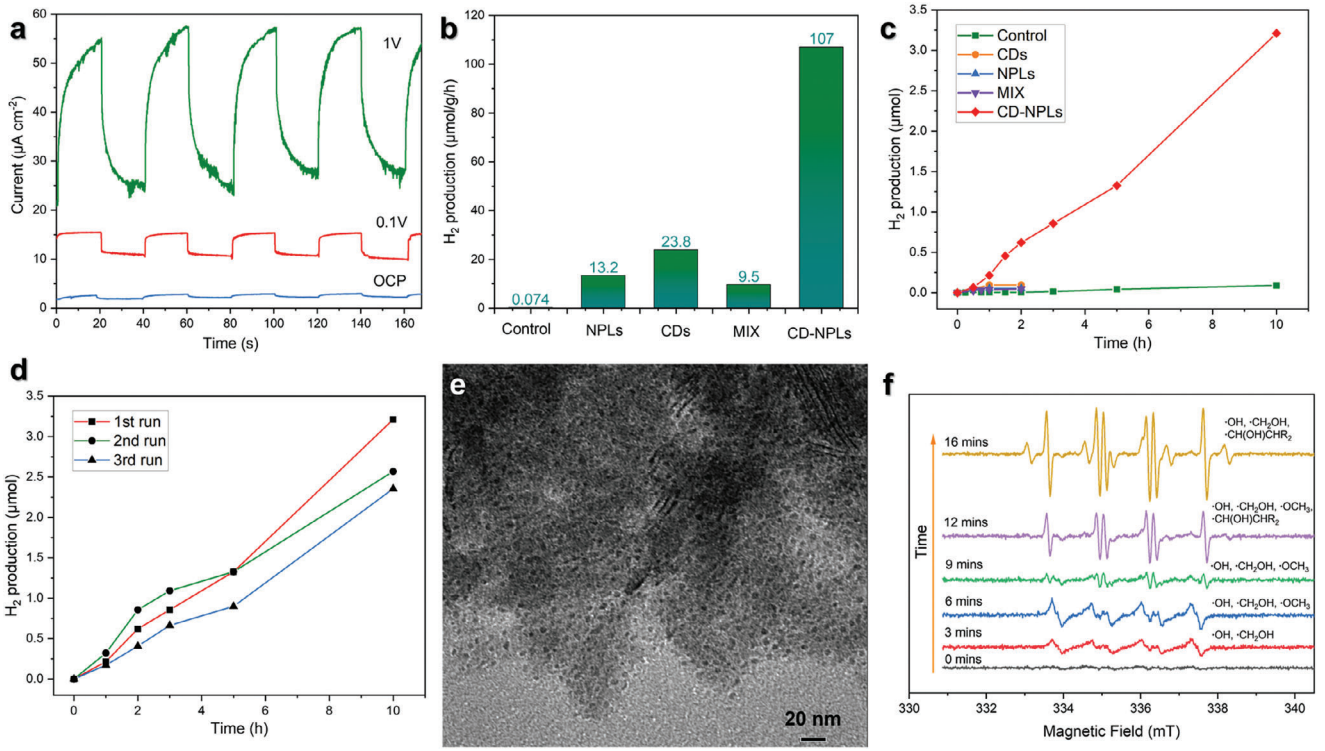

Figure 6. Photocatalytic performance of colloidal CD-NPLs heterostructures. (a) Baseline-corrected photocurrent densities curves of the CD-NPLs at open circuit potential (OCP) and different bias potentials (0.1 and 1 V) under chopped illumination in 0.1 M KOH methanol solution. (b) Hydrogen production performance of blank control, NPLs, CDs, mixture of CDs and NPLs, and CD-NPLs at one hour. (c) Time-dependent curve of hydrogen production performance of blank control, NPLs, CDs, mixture of CDs and NPLs, and CD-NPLs. (d) The cyclic hydrogen production performance of CD-NPLs. (e) HRTEM of CD-NPLs after 10 hrs photocatalysis. (f) In situ X-band electron paramagnetic resonance spectroscopy (EPR) under spin traps of 5, 5-dimethyl-1-pyrroline N-oxide (DMPO) at different time of the reaction.

Efficiency (AQE) of be 6.03% (λ = 365 nm). For the long-term run, after 10 hours, the CD-NPLs reach 3.21 μmol, Figure 6b. The CD-NPLs demonstrate an increased efficiency, benefitting from the ultrafast interfacial charge transfer and long electron-hole separation across the vdW heterojunction. Furthermore, the recycling experiment also found that the photocatalytic efficiencies remain stable in all three runs, each for 10 h, Figure 6d. The CD-NPLs demonstrate a significant promotion not only on efficiency but also on stability during photocatalysis. The HRTEM image of the CD-NPLs particles collected after photocatalysis, Figure 6e, shows that the CDs are still clearly discernible on the ZnSe NPLs after the light excitation and the reaction. The colloidal heterostructure photocatalyst demonstrates resistance to photocorrosion in maintaining their catalytic activity.

To understand the transformation during the methanol decomposition, in situ X-band (9.6 GHz) electron paramagnetic resonance spectroscopy (EPR) was used in conjunction with the spin trap DMPO to track the generation of radicals over 180 minutes. The spectra show a complicated set of signals that comprise at least four major EPR components, following the reaction time as shown in Figure 6f and Figure S12 (Supporting Information). Simulation of these data using a nitrogen and proton hyperfine coupling yielded the values C1 (A_N = 13.0 G, A_H = 14.7 G), C2 (A_N = 15.0 G, A_H = 21.2 G), C3 (A_N = 9.6 G, A_H = 7.8 G), C4 (A_N = 12.2 G, A_H = 13.7 G), C5 (A_N = 13 G, A_H = 8.8 G), Figure S12 (Supporting Information). In spin trap experiments with DMPO, where the hyperfine couplings are known to depend upon the solvent polarity and for methanol, the signals were assigned as C1 is •OH, C2 to •CH_2OH, C4 to •$CH(OH)CHR_2$, C5 to •CH_3O radicals, and C3 to a very low nitrogen hyperfine reaction is likely a ring-opening decay product of DMPO. Therefore, the methanol splitting started with rich amounts of •CH_3O radical at the beginning (Figure S12a, Supporting Information for the 6 min reaction) and stabilized with the •CH_2OH radical (Figure S12b, Supporting Information for the 16 mins reaction). For the longer time reaction, the •$CH(OH)CHR_2$ signal was also found to co-exist with •CH_2OH and •CH_3O (Figure S12c, Supporting Information for 162 mins reaction), suggesting the co-existence of reaction Pathway 1 and 2 depicted in Figure 1d. It is known that C–H bond splitting is more difficult than O-H splitting.[9] The ability of CD-NPLs C–H splitting and C–C bond formation (as exhibited by C4) demonstrate the unique pathway for the heterostructure catalyst design for methanol photo-reforming reactions. Though the hydrogen production rate of this work is not yet the highest in the recent literature, the ability of CD-NPLs in catalyzing α-C–H splitting and C–C coupling is extraordinary. **Table 1** below shows a comparison among recent studies on the performance of photocatalysts on methanol-storage hydrogen.

Nuclear magnetic resonance (NMR) further confirmed the intermediate radicals. As shown in Figure S13 (Supporting Information), there are 2 new peaks detected in the 24 hours sample with a broad singlet peak at 4.48 ppm and a triplet peak at

Table 1. A comparison of new catalysts performance regarding COx-free, photocatalytic production of methanol-storable hydrogen.

Catalyst	Hydrogen production rate	C–C coupling	Refs.
MgO nanoparticles	320 μmole·g^{-1}·h^{-1}	No	[3]
MoS_2 single-layer nanosheets	617 μmole·g^{-1}·h^{-1}	No	[7]
MoS_2-foam-modified CdS nanorods	12000 μmole·g−1·h−1	Yes	[8]
CD-ZnSe NPLs	107 μmole·g−1·h−1	Yes	This work

4.37 ppm (coupling constant around 5.61 Hz). The second peak is a C–H and the triplet signal indicates that it attaches to -CH_2 with the same chemical environment, which is generated from the reaction. Its downfield chemical shift indicates that the CH proton is attached to electronegative groups. In Figure S13 (Supporting Information), few very downfield peaks appeared in the 24 h sample, peaks around 9 -10 ppm, which is consistent with aldehyde hydrogens. This indicates the existence of intermediate aldehyde (CH_2OH). The new peaks at 7.6, 7.8, 7.9 ppm correspond to the presence of aromatic protons associated with the CD aromatic rings. The resident photogenerated holes in the CDs will generate the majority of •CH_2OH, which leads to the formation of ethylene glycol (pathway 1 in Figure 1d). The multiple peaks at 2.6-2.7 ppm move downfield over time, corresponding to the exchangeable protons of OH. No CO_x was detected in either the gas or liquid phase of the photocatalytic reaction system, demonstrating a promising future application for zero-carbon-emission hydrogen release.

In conclusion, we have successfully developed an organic-inorganic heterostructure quantum material synthesis method, forming highly crystalline CDs of a diameter 3 ± 1 nm on ZnSe NPLs of dimensions of 50 × 16 × 1.39 nm. The key to this CDs in situ growth on the metal chalcogenide NPLs is in the ligand mediated, localized graphitization of carbon precursors. Physiochemical and optical characterizations demonstrate that the CDs are firmly attached on the planar surface and the edges of ZnSe NPLs, whereas the DFT computations suggest an interfacial distance of 0.24 nm. TA spectroscopy, and the combination of steady-state and time-resolved PL analyses revealed the interfacial charge transfer in the colloidal CD-ZnSe NPLs heterostructures, whereby the CDs are the electron donors under light excitation, and that the charge transfer from CDs to ZnSe NPLs takes place within 500 ps, resulting in electron-hole separation extended to hundreds of nanoseconds. The CD-ZnSe NPL heterostructure shows significantly improved photocatalytic activity; under ambient conditions, the photocatalytic methanol dehydrogenation reaction reached the highest productivity in the presence of CD-ZnSe NPLs at 107 μmole·g^{-1}·h^{-1}, more than four times as much as CDs on their own, which demonstrates the effect of photo-induced charge transfer in this heterostructure. High photocurrent of a 0.8 μA cm^{-2} at OCP, 5 μA cm^{-2} at 0.1 V and 34 μA cm^{-2} at 1 V was achieved. Radical analysis with EPR spectroscopy and final liquid product analysis with NMR shows considerable generation of •CH_2OH and the likelihood of C–C bond formation. The organic-inorganic heterostructure catalyst design provides new routes for tuning the photocatalytic redox energy level and the surface property heterogeneity for driving selective catalytic reaction pathways. The new method introduced here for synthesizing novel 0D-2D, pseudo 2D-2D vdW heterostructure quantum materials with eco-friendly materials such as CDs and ZnSe can enable the discovery of a host of novel nano-hybrid materials for wide applications including photocatalysis, sensing, and opto-electronic devices.

Supporting Information

Supporting Information is available from the Wiley Online Library or from the author.

Acknowledgements

The authors acknowledge the financial support from the Australian Research Council with ARC Industry Transformation Research Hub IH 180100002, ARC Discovery Projects: DP 200101105, DP230102192, Griffith University New Researcher Grant and Australian Synchrotron project (AS221/SXR/18411). R.J.H. and T.A.S. were supported by the ARC Centre of Excellence in Exciton Science (CE170100026), the ARC Linkage, Equipment and Facilities Scheme (LE200100051) and the Australian Centre for Advanced Photovoltaics (ACAP) Infrastructure Scheme. This work was performed in part at the Queensland node of the Australian National Fabrication Facility, a company established under the National Collaborative Research Infrastructure Strategy to provide nano- and micro-fabrication facilities for Australia's researchers. The authors acknowledge the facilities, and the scientific and technical assistance, of the Australian Microscopy & Microanalysis Research Facility at the Centre for Microscopy and Microanalysis, the University of Queensland.

Open access publishing facilitated by Griffith University, as part of the Wiley - Griffith University agreement via the Council of Australian University Librarians.

Conflict of Interest

The authors declare no conflict of interest.

Data Availability Statement

The data that support the findings of this study are available from the corresponding author upon reasonable request.

Keywords

carbon dots, colloidal synthesis, hybrid nanoparticles, methanol oxidation, photocatalysis

Received: April 11, 2024
Revised: May 28, 2024
Published online: June 8, 2024

[1] M. D. Allendorf, V. Stavila, J. L. Snider, M. Witman, M. E. Bowden, K. Brooks, B. L. Tran, T. Autrey, *Nat. Chem.* **2022**, *14*, 1214.
[2] J. O. Abe, A. P. I. Popoola, E. Ajenifuja, O. M. Popoola, *Int. J. Hydrogen Energy* **2019**, *44*, 15072.
[3] Z. Liu, Z. Yin, C. Cox, M. Bosman, X. Qian, N. Li, H. Zhao, Y. Du, J. Li, D. G. Nocera, *Sci. Adv.* **2016**, *2*, 1501425.

[4] X. Bai, D. Yuan, Y. Li, H. Song, Y. Lu, X. San, J. Lu, G. Fu, S. Wang, J. Ye, *iScience* **2021**, *24*, 102056.
[5] G. A. Olah, *Angew. Chem., Int. Ed.* **2005**, *44*, 2636.
[6] F. Wang, R. Swinbourn, C. Li, *Int. J. Hydrogen Energy* **2023**, *48*, 14763.
[7] Y. Pang, M. N. Uddin, W. Chen, S. Javaid, E. Barker, Y. Li, A. Suvorova, M. Saunders, Z. Yin, G. Jia, *Adv. Mater.* **2019**, *31*, 1903998.
[8] D. Gunawan, J. A. Yuwono, P. V. Kumar, A. Kaleem, M. P. Nielsen, M. J. Y. Tayebjee, L. Oppong-Antwi, H. Wen, I. Kuschnerus, S. L. Y. Chang, Y. Wang, R. K. Hocking, T. S. Chan, C. Y. Toe, J. Scott, R. Amal, *Appl. Catal. B Environ.* **2023**, *335*, 122880.
[9] S. Xie, Z. Shen, J. Deng, P. Guo, Q. Zhang, H. Zhang, C. Ma, Z. Jiang, J. Cheng, D. Deng, Y. Wang, *Nat. Commun.* **2018**, *9*, 1181.
[10] K. Chen, F. Wang, Y. Wang, F. Zhang, X. Huang, J. Kang, Q. Zhang, Y. Wang, *JACS Au* **2023**, *3*, 2894.
[11] T. Dalton, T. Faber, F. Glorius, *ACS Cent. Sci.* **2021**, *7*, 245.
[12] L. Lin, Q. Yu, M. Peng, A. Li, S. Yao, S. Tian, X. Liu, A. Li, Z. Jiang, R. Gao, X. Han, Y. W. Li, X. D. Wen, W. Zhou, D. Ma, *J. Am. Chem. Soc.* **2021**, *143*, 309.
[13] M. Latorre-Sánchez, A. Primo, H. García, *Angew. Chem., Int. Ed.* **2013**, *52*, 11813.
[14] Z. Lian, Y. Kobayashi, J. J. M. Vequizo, C. S. K. Ranasinghe, A. Yamakata, T. Nagai, K. Kimoto, K. Kobayashi, K. Tanaka, T. Teranishi, M. Sakamoto, *Nat. Sustain.* **2022**, *5*, 1092.
[15] X. Uddin, Z. Sun, J. Langley, H. Lu, P. Cao, A. Wibowo, X. Yin, C. S. Tang, H. T. Nguyen, J. D. Evans, X. Li, *Proc. Natl. Acad. Sci.* **2017**, *120*, 2017.
[16] S. Xie, W. Ma, X. Wu, H. Zhang, Q. Zhang, Y. Wang, Y. Wang, *Energy Environ. Sci.* **2021**, *14*, 37.
[17] C. Xia, S. Zhu, T. Feng, M. Yang, B. Yang, *Adv. Sci.* **2019**, *6*, 1901316.
[18] B. Jana, Y. Reva, T. Scharl, V. Strauss, A. Cadranel, D. M. Guldi, *J. Am. Chem. Soc.* **2021**, *143*, 20122.
[19] S. Wang, I. S. Cole, D. Zhao, Q. Li, *Nanoscale* **2016**, *8*, 7449.
[20] Z. Zhang, G. Yi, P. Li, X. Zhang, H. Fan, Y. Zhang, X. Wang, C. Zhang, *Nanoscale* **2020**, *12*, 13899.
[21] J. Liu, Y. Liu, N. Liu, Y. Han, X. Zhang, H. Huang, Y. Lifshitz, S. Lee, J. Zhong, Z. Kang, *Science* **2015**, *347*, 646.
[22] S. Wang, I. S. Cole, Q. Li, *ChemComm* **2016**, *52*, 9208.
[23] A. K. Ciarrocchi, F. Tagarelli, A. Avsar, *Nat. Rev. Mater.* **2022**, *7*, 449.
[24] Y. Ben-Shahar, D. Stone, U. Banin, *Chem. Rev.* **2023**, *123*, 3790.
[25] Y. Nakibli, P. Kalisman, L. Amirav, *J. Phys. Chem. Lett.* **2015**, *6*, 2265.
[26] Y. Nakibli, Y. Mazal, Y. Dubi, L. Amirav, *J. Phys. Chem. Lett.* **2018**, *18*, 357.
[27] U. Banin, Y. Ben-Shahar, K. Vinokurov, *Chem. Mater.* **2014**, *26*, 97.
[28] C. Ye, D. S. Zhang, B. Chen, C. H. Tung, L. Z. Wu, *ACS Cent. Sci.* **2024**, *10*, 529.
[29] D. Chen, A. Wang, M. A. Buntine, G. Jia, *ChemElectroChem* **2019**, *6*, 4709.
[30] D. Chen, H. Zhang, Y. Li, Y. Pang, Z. Yin, H. Sun, L. C. Zhang, S. Wang, M. Saunders, E. Barker, G. Jia, *Adv. Mater.* **2018**, *30*, 1803351.
[31] Y. Pang, M. Zhang, D. Chen, W. Chen, F. Wang, S. J. Anwar, M. Saunders, M. R. Rowles, L. Liu, S. Liu, A. Sitt, C. Li, G. Jia, *J. Phys. Chem. Lett.* **2019**, *10*, 3465.
[32] F. Wang, S. Pang, L. Wang, Q. Li, M. Kreiter, C. Y. Liu, *Chem. Mater.* **2010**, *22*, 4528.
[33] D. Chen, M. U. Zia, F. Yang, Y. Wang, F. D. L. Leusch, N. T. Nguyen, W. Zhang, Y. Gao, D. Zhao, C. L. Raston, Q. Li, *ACS Sustainable Chem. Eng.* **2023**, *11*, 11756.
[34] L. Liu, B. Bai, X. Yang, Z. Du, G. Jia, *Chem. Rev.* **2023**, *123*, 3625.
[35] H. Fu, D. Yang, D. Qiu, C. H. Yan, R. Cai, Y. Du, W. Tan, *J. Phys. Chem. Lett.* **2022**, *13*, 1855.
[36] W. Chen, X. Li, F. Wang, S. Javaid, Y. Pang, J. Chen, Z. Yin, S. Wang, Y. Li, G. Jia, *Small* **2020**, *16*, 1902231.
[37] D. Chen, A. Wang, H. Li, L. Abad Galán, C. Su, Z. Yin, M. Massi, A. Suvorova, M. Saunders, J. Li, A. Sitt, G. Jia, *Nanoscale* **2019**, *11*, 10190.
[38] A. Wang, W. Wang, J. Chen, R. Mao, Y. Pang, Y. Li, W. Chen, D. Chen, D. Hao, B. J. Ni, M. Saunders, G. Jia, *J. Phys. Chem. Lett.* **2020**, *11*, 4990.
[39] S. Mourdikoudis, L. M. Liz-marza, *Chem. Mater.* **2013**, *25*, 1465.
[40] V. A. Shchukin, D. Bimberg, *Rev. Mod. Phys.* **1999**, *71*, 1125.
[41] I. V. Markov, *Crystal Growth and Epitaxy*, World Scientific, Singapore **2016**.
[42] A. Kuznetsova, I. Popova, J. T. Yates, M. J. Bronikowski, C. B. Huffman, J. Liu, R. E. Smalley, H. H. Hwu, J. G. Chen, *J. Am. Chem. Soc.* **2001**, *123*, 10699.
[43] S. Kishida, K. Matsuura, H. Mori, T. Yanagawa, I. Tsurumi, C. Hamaguchi, *Phys. Status Solidi* **1988**, *106*, 283.
[44] V. V. Matylitsky, A. Shavel, N. Gaponik, A. Eychmüller, J. Wachtveitl, *J. Phys. Chem. C* **2008**, *112*, 2703.
[45] R. Costi, G. Cohen, A. Salant, E. Rabani, U. Banin, *Nano Lett.* **2009**, *9*, 2031.
[46] F. Yuan, T. Yuan, L. Sui, Z. Wang, Z. Xi, Y. Li, X. Li, L. Fan, Z. Tan, A. Chen, M. Jin, S. Yang, *Nat. Commun.* **2018**, *9*, 2249.